Check for updates

Yttrium and REE Mineralization in Manganese Pods Occurring in Bentonite Deposits of the Eocene Texas Coastal Plain

Debora Berti [ID] · Niall C. Slowey · Youjun Deng · Thomas E. Yancey [ID] · Ana L. Barrientos Velazquez [ID]

Abstract Eocene-aged bentonite deposits in Gonzalez (Texas, USA) carrfy scattered manganese oxide-rich pods where rare earth element (REE) concentrations as high as 7800 ppm have been detected — 10 times greater than in the already enriched bentonite. This study investigated the nature of the association between REEs and Mn oxides as well as REE modes of occurrence in these pods, in order to understand the processes that mobilize and accumulate REEs in the low-temperature depositional environment of the Texas coastal plain. Embedded, polished blocks of Mn pods were analyzed by Scanning Electron Microscopy (SEM); sections were then extracted by the FIB liftout technique from regions bearing REEs for further analysis by Transmission Electron Microscopy (TEM). The SEM and TEM results revealed the presence of abundant yttrium phosphate nanoparticles identified as xenotime, forming large globular aggregates that reach a few microns in diameter; these xenotime aggregates also host trace concentrations of Zr, Dy, Er, Yb, and Ce. Further, rhabdophane nanoparticles were detected that host predominantly light REEs and Y. The relative proportions of REEs in rhabdophane vary between particles and show decoupling of Ce from other light REEs, suggesting oxidation from Ce^{3+} to Ce^{4+}. The REE enrichment of these Mn pods is due to extensive weathering along fractures cutting through the bentonite deposit that drove their remobilization and transport downward. At the base of the bentonite, where fractures terminate against the boundary with a cemented sandstone, changes in flow regime combined with gradual downward changes in fluid composition, prompted co-precipitation of Mn oxides and REE phosphates (xenotime and rhabdophane).

D. Berti (✉) · N. C. Slowey
Department of Oceanography, Texas A&M University, College Station, TX 77843, USA
e-mail: debora-berti@tamu.edu

Y. Deng · A. L. B. Velazquez
Department of Soil and Crop Sciences, Texas A&M University, College Station, TX 77843, USA

T. E. Yancey
Department of Geology and Geophysics, Texas A&M University, College Station, TX 77843, USA

Introduction

Eocene-aged sediments of the Texas coastal plain contain numerous, widespread rhyolitic ash layers

🖄 Springer

that are exposed along a southwest-northeast corridor, ~ 70 km inward of the current coastline (Fig. 1). Near the Eocene coastline in central Texas, a strand-plain-barrier depositional system provided local conditions favorable to the alteration of volcanic ash into thick bentonite deposits that have been mined in Gonzalez (Texas, USA) for over a century (Chen, 1968; Fisher et al., 1970; Heintz et al., 2015; Roberson, 1964; Yancey & Guillemette, 1998; Yancey et al., 2018). Volcanic glass conversion into montmorillonite — the main mineral of these bentonite deposits — is driven by interaction with brackish water; silica and alkali leach from the glass while nucleation and growth of montmorillonite leads to the enrichment of Al, Mg, and Ca relative to the parent ash (Galloway, 1978; Zielinski, 1982; Senkayi et al., 1984; Christidis, 1998). Leaching also leads to accumulation of immobile or less mobile elements (e.g. Ti) in the altered ash deposit and the release of others into pore water (Galloway, 1978; Zielinski, 1982; Senkayi et al., 1984; Christidis, 1998).

Texas bentonite deposits accumulated rare earth elements, the lanthanides of the periodic table and yttrium (REE), where the ionic radius of Y is between those of Dy and Ho. Published data report total concentrations up to 600 ppm, in strata up to 6 m thick (Michaelides, 2011), with REEs hosted in secondary phosphate nanominerals that formed with montmorillonite during the aqueous alteration of volcanic ash (Berti et al., 2022). Further, these deposits contain favorable proportions of REEs that are critical (Nd, Eu, Tb, Dy, Y, Er) for current technologies and are limited in supply (Dai & Finkelman, 2018; Seredin & Dai, 2012). Indeed, altered volcanic ash is an important source of REEs in coal deposits (e.g. Dai & Finkelman, 2018; Dai et al., 2017; Hower et al., 2018; Liu et al., 2019), late Permian bentonite horizons in Yunnan province of China (Shen et al., 2021; Zhao et al., 2017), and also tuff in the Heling deposit, one of the regolith-hosted ores that supplies REEs to most of the world market (Bao & Zhao, 2008; Li et al., 2020).

Some of the Texas Eocene bentonite deposits show a yellow hue due to the presence of ferromanganese (oxyhydr) oxide veins, varnishes, and host characteristic Mn oxide-rich pods that are close to
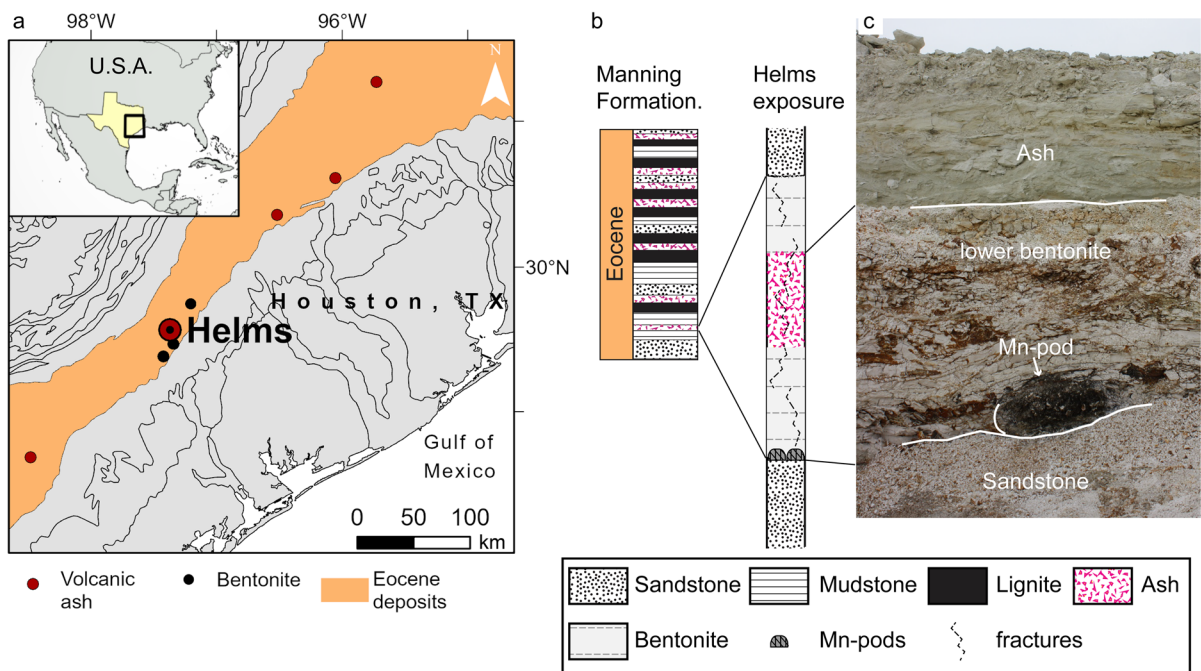
Fig. 1 Location of the Helms pit and stratigraphy of the bentonite deposit. **a** Geological map of the Eocene coastal deposits where black circles mark locations of bentonite deposits, red circles mark locations of Eocene ash layers outcrops. **b** Stratigraphic column of the late Eocene Manning Fm. (Yancey & Guillemette, 1998) and of the bentonite deposit exposed at Helms pit. **c** Picture of the Helms deposit exposure showing a Mn pod at its base

1 m in diameter and in which preliminary investigations identified anomalously high REE concentrations (7800 ppm REE, this study). Associations of ferromanganese nodules and crusts with anomalous concentrations of REEs are not uncommon (though usually at smaller concentrations); in marine settings, some of these associations have been linked to scavenging from seawater, hydrothermal circulation, or phosphatization events (Bau et al., 1996, 2014; Conrad et al., 2017; Kuhn et al., 1998; Sasmaz et al., 2020, 2021). Enriched REE intervals also form in marine and lake sediments post deposition by release of adsorbed REEs during reduction of Fe–Mn (oxyhydr)oxides (e.g. Och et al., 2014). However, Fe–Mn (oxyhydr)oxides are not always associated with enrichment of REEs; for instance, no association was found between Fe–Mn (oxyhydr)oxides and REEs in the Chinese regolith deposits that are one of the world's main sources (Li et al., 2020). Among REEs, Ce has the strongest association with Fe–Mn deposits because of similar redox behavior (Bau et al., 2014; Conrad et al., 2017) and can be scavenged oxidatively by particulate Fe–Mn oxides (Bau and Koschinsky, 2009) whereas the aqueous behavior of other REEs is more affected by the presence of ligands (e.g. Cl^-, SO_4^{2-}, F^-, CO_3^{2-}) and reactive surfaces, both being pH dependent (Cao et al., 2001; Cetiner et al., 2005; Migdisov et al., 2016; Poitrasson et al., 2004). Prolonged weathering can remobilize REEs from easily alterable components of a deposit and the different aqueous behavior of REEs result, over long periods of time, in their fractionation along the depth profile or groundwater path. In particular, Ce oxidizes from tri- to a tetravalent form that precipitates in authigenic minerals, thereby resulting in a Ce concentration spike at the oxidation front and consequent subtraction from leaching solution (Bao & Zhao, 2008; Li et al., 2020).

For the Eocene-aged bentonites of the Texas coastal plain, deciphering the nature of the REE association with Mn oxides as well as their modes of occurrence is crucial for understanding low-temperature processes that mobilize and fractionate REEs in coastal settings, their relation to the volcanic ash, and their economic potential. These bentonite deposits are comparable to other weathering-type deposits in the USA (e.g. Cheshire et al., 2018; Elliott et al., 2018; Hower et al., 2018; Pingitore et al., 2018) for which mineral-specific REE extraction

technologies are being developed (Dai & Finkelman, 2018; Stuckman et al., 2018; Wanhala et al., 2019).

The objective of the present study was to investigate the occurrences of REEs associated with pods of Mn oxides found at the base of bentonite-altered ashfall deposits in Gonzales County, Texas, USA to ascertain their association with Mn oxides and the processes that led to their accumulation.

Geological Setting

The middle–late Eocene to early Oligocene stratigraphic record of the Texas coastal plain is marked by numerous volcanic ash layers that are exposed along the Eocene paleo-coastline, ~70 km landward of the current coastline (Fig. 1). These layers occur most frequently in the late-Eocene Manning Formation, where they interbed with alternating layers of sandstones and mudstones that compose para-sequences of multiple transgressive–regressive cycles of sea-level (Fig. 1b). High frequency depositional cycles are superimposed on an overall regressive sea-level trend, reflecting a change in global climate conditions from warm to cool. Each ash bed is typically in sharp contact with surrounding sedimentary deposits and is laterally extensive. Indeed, a few ash beds have been traced along the Gulf Coast in Texas (Yancey & Guillemette, 1998) and as far as Louisiana and Mississippi (Jordan et al., 2019).

Previous studies determined the volcanic ash has a rhyolitic, subalkaline composition and originates from the Sierra Madre Occidental volcanic field (Guillemette & Yancey, 1996; Heintz et al., 2015; Michaelides, 2011; Yancey et al., 2018) where ignimbrite flare-up episodes in the late Eocene emitted large volumes of volcanic ash into the atmosphere (Ferrari et al., 2018; Yancey et al., 2018). Ash clouds were transported eastward over distances exceeding 1000 km to the Texas gulf coast and as far as Mississippi (Yancey & Guillemette, 1998; Yancey et al., 2018). Near Gonzalez (Texas), volcanic ash settled in marine or brackish environments where it subsequently altered — partially or completely — into thick deposits of bentonite (some exceeding 6 m in thickness) that have been important economically for over a hundred years.

In all known deposits, the bentonite is composed largely of montmorillonite (80–95%) with a smaller fraction (0–20%) of opal-C, that acts as a cement, and a small fraction (0 to 5%) of coarser phenocrysts, including feldspars (mostly sanidine), zircon, titanite, biotite, and quartz (Berti et al., 2022; Chen, 1968; Chipera & Bish, 2001; Henderson et al., 1971; Michaelides, 2011; Roberson, 1964). Chen (1968) and Roberson (1964) described different lithotypes for the Gonzalez bentonites, based on coloration and hardness; coloration varies between blue that is due to the presence of pyrite, white from bentonite formed in a well oxygenated environment, and yellow from iron oxide-stained fractures. Soft and hard intervals are recognized with greater hardness reflecting the presence of opal-C cement.

The Helms pit in Gonzalez exposes an approximately 4 m thick ashfall deposit that is altered fully into bentonite at the top and bottom but comprises a less altered, ash-rich middle section. Sharp boundaries separate the ashfall deposit from an overlying sandstone layer and an underlying cemented sandstone layer. This deposit age is 35.67 ± 0.05 Ma, based on $^{40}Ar/^{39}Ar$ dating of single sanidine phenocrysts and is coeval with the bentonite at the nearby H. W. Johnson pit (Yancey et al., 2018) which shows similar REE enrichment (Berti et al., 2022). The top portion of the ashfall deposit (~ 1 m thick) is hard white bentonite, the mid-section is a mixture of bentonite and volcanic glass shards, whereas the bottom of the deposit is heavily fractured bentonite that exhibits a yellow hue, deriving from Fe (oxyhydr)oxide crusts on fracture walls. Within the Fe (oxyhydr)oxide crusts, Mn oxides are rare and in minor concentrations. However, well developed Mn oxide intervals occur at the top and bottom boundaries of the bentonite layer. Remarkably, large concentrations of Mn oxides are found at the base of the ashfall deposit (on top of a cemented sandstone), in pods characterized by a mound shape, with a diameter ranging between 80 and 120 cm and a height of ~ 50 cm. The patchy lateral distribution of the pods indicates their association with the set of fractures that cut through (otherwise impermeable) bentonite, thus opening preferential paths for water downward flow.

Materials and Methods

Samples

Samples were collected from freshly exposed surfaces of several Mn pods at the base of the ashfall deposit exposed at the Helms pit in Gonzales, Texas (Lat. 29.484340^0N, Lon. 97.370987^0W) and surveyed by XRD and by ICP-MS (limited set of elements). Based on preliminary data, two Mn pod samples (Mn13-03, Mn14-01) were selected for electron microscopy investigation. Additionally, samples collected from the top and bottom bentonite (B13-08, B13-04), from the intervening ash interval (V13-01), and > 20 μm sized glass shards separated from the ash interval (V13-01 > 20 μm) were analyzed by ICP-MS and SEM.

Chemical Composition of Major, Trace, and RE Elements

Samples were ground using an agate mortar and pestle until >95% of the sample passed a #140 mesh sieve. Splits of the ground, homogenized samples were sent to Activation Laboratories, Ltd. (Ancaster, Ontario, Canada) for elemental analysis by ICP-OES or ICP-MS. Samples and a blank were processed by lithium metaborate/tetraborate fusion to ensure complete fusion, then digested in weak nitric acid solution prior to analysis by ICP-MS for Cr, Co, Ni, Cu, Zn, Ga, Ge, As, Rb, Nb, Mo, Ag, In, Sn, Sb, Cs, REY, Hf, Ta, W, Tl, Pb, Bi, Th, and U and by ICP-OES for major element oxides, Sc, Be, V, Ba, Sr, Y, and Zr. Accuracy and precision were ensured by calibration with 14 certified USGS and CANMET standards.

The chemical index of alteration (CIA), defined as the ratio of Al and the sum of Al and alkali (Nesbitt & Young, 1982), was calculated from the ICP-OES data as: $Al_2O_3/(Al_2O_3 + K_2O + CaO + Na_2O)$ in percent. The Ce anomaly (Ce/Ce*) was calculated using concentrations normalized to the Upper Continental Crust (UCC, McLennan, 2001) using the geometrical mean method: $Ce/Ce* = Ce/\sqrt{(La \bullet Pr)}$; similarly, the Eu anomaly (Eu/Eu*) was calculated using UCC normalized concentrations as: $Eu/Eu* = Eu/\sqrt{(Sm \bullet Gd)}$. Additionally, the proportion of critical over total REEs ($REE_{def,rel}$) and the outlook coefficient (C_{out}) were calculated

as: $REE_{def,rel} = (Nd + Eu + Dy + Tb + Y + Er)/\sum REE$ and $C_{out} = (Nd + Eu + Dy + Tb + Y + Er)/(Ce + Ho + Tm + Yb + Lu)$.

Powder X-ray Diffraction

A portion of the bulk samples was treated to separate the sand, silt, and clay fractions using the procedures of Deng et al. (2013). The mineralogical characterization of the ground bulk samples splits as well as its silt and clay fractions was performed using a D8 Bruker Advance diffractometer (Bruker AXS, Karlsruhe, Germany) with a 1-D position sensitive LynxEye detector (Bruker AXS, Karlsruhe, Germany) and CuKα radiation, operated at 35 kV and 45 mA. Additionally, XRD patterns of the clay fraction were acquired after Mg-saturation, glycerol solvation, K-saturation at room temperature, and after heating treatments at 300 and 550°C.

Scanning Electron Microscopy

Sample blocks for SEM analysis were prepared by dehydration and embedding, using a four-component epoxy resin that combines the stability and polishing quality of Araldite 502 with the low-viscosity and water-forgiving properties of Quetol 601 (Ellis, 2016), using chemicals manufactured by Electron Microscopy Sciences (Hatfield, Pennsylvania, USA). One surface of the embedded blocks was polished using diamond lapping films with sequentially finer grit size, ending at a grit size of 0.1 µm. After carbon coating, the flat, polished block surfaces were analyzed using a Tescan LYRA-3 high-resolution dual-beam FIB-SEM (Tescan, Kohoutovice, Czech Republic), equipped with an Oxford Instruments silicon drift detector for EDS (Oxford Instruments Nanoanalysis, Concord, Massachusetts, USA), and a dedicated backscatter electron (BSE) detector (Tescan, Kohoutovice, Czech Republic) mounted on the polepiece of the electron beam column. BSE images — for which contrast is a function of average atomic number — were collected at beam energies of 10 and 5 keV. Voltage was increased to 15 keV for EDS analysis to provide sufficient overvoltage for the detection of most elements while maintaining a spatial resolution of ~1 µm. The Oxford Instruments *AZtec®* software was used to identify elements in the EDS spectra and for standardless quantification. SEM analysis

identified REE hosted in nanoparticulates for which the SEM–EDS spatial resolution is not sufficient to characterize the chemical composition adequately; therefore, a few representative sites were chosen for further analysis by TEM. Sections suitable for TEM analysis were extracted from the selected sites using the FIB liftout technique (Giannuzzi, et al., 1998) and the same FIB-SEM instrument. With this technique, a section (~10 µm long, 5 µm deep) through the region of interest was exposed by ion milling trenches on either side, then extracted with the aid of a micro-manipulator and soldered (using Pt) on a TEM grid holder; finally, the in situ section was made ready for TEM by thinning it to electron transparency (~0.1 µm) using the ion beam.

Transmission Electron Microscopy

In situ sections prepared by FIB liftout were analyzed using a Tecnai G20 TEM (Thermo Fisher Scientific Inc., Waltham, Massachusetts, USA) with an Oxford Instruments EDS detector (Oxford Instruments Nanoanalysis, Concord, Massachusetts, USA), operated at 200 keV. Because the spatial resolution of TEM-EDS analysis is controlled by the size of the beam (Cliff & Lorimer, 1975), EDS spectra were acquired in scanning mode (STEM), by focusing the beam to a spot size ranging between 30 nm and ~1 nm (depending on operating conditions and magnification). In the same mode and conditions, atomic contrast images were acquired using a High Angle Annular Dark Field (HAADF) electron detector (Thermo Fisher Scientific Inc., Waltham, Massachusetts, USA). Mineral identification was based on chemical composition determined by EDS in combination with crystal structure parameters determined from selected area diffraction patterns (SAED) and from high-resolution TEM images (HRTEM). For HRTEM images, lattice parameters were measured from their corresponding fast fourier transform (FFT) which was computed using Gatan Microscopy Suite (GMS 3.5) software.

Results

Major Elements and REE Concentrations

The major- and trace-element compositions of the ashfall deposit and of the manganese pods

☰ Springer

(Supplementary Table S1) showed that the aqueous alteration of volcanic ash into bentonite results in a loss of silica and alkali, as well as uptake of Mg from seawater. The degree of alteration, quantified by the CIA, displayed a minimum of 55% in the sorted ash — which is in good agreement with the value expected for rhyolitic composition — and increased to a maximum of 77% in the bentonite intervals, corresponding to the progressive alteration from the mid-section toward the top and bottom of the deposit. In the Mn pods, the CIA was slightly lower than in the bentonite, due to the presence of Ca in the manganese minerals (as shown by SEM–EDS) rather than a lower degree of alteration.

In the pods, the Mn oxide concentration ranged from 20.75 to 24.5%, as opposed to ~0.06% in the midsection of the ashfall deposit and ~0.013% in the top and bottom bentonite intervals. Additionally, the iron concentration in pods was twice that of the ashfall deposit but remained low (~2%), yielding a Mn/Fe ratio of ~9. Concentrations of other major elements also differed from those in the ash, revealing less SiO_2, an order of magnitude more P (mean of 0.3% versus 0.03% for ash), slightly more Ca, and less Mg. Compared to the composition of the volcanic ash, the Mn pods showed anomalously high concentrations of several trace elements (Supplementary Table S2, Supplementary Fig. S1): Ba, Zn, Ni, Sr, Co, V, Mo, As, Ga, Cu, Sb, Tl, and U (ordered from high to low concentration); high concentrations of REEs; and depletion of Rb, Cs, W, and Zr.

The concentration of REEs in the Helms ashfall deposit was high (Table 1), reaching a maximum of 730 ppm in the meter-thick mixed ash-clay interval. This value is the highest concentration reported so far for the Gonzalez bentonite deposits (Berti et al., 2022; Heintz et al., 2015; Michaelides, 2011). Remarkably, the REE concentration increased ten-fold in the Mn pods where it ranged between 7100 and 7838 ppm. The Ba/Eu ratio remained well below the 1000 threshold above which quantification of Eu by ICP-MS is not considered reliable (Yan et al., 2018).

The relative proportions of light REE (LREE: La–Sm), medium REE (MREE: Eu–Dy + Y), and heavy REE (HREE: Ho–Lu) also changed between the ashfall deposit and the Mn pods, as illustrated in Fig. 2 by the trends of REE concentrations normalized to the UCC (McLennan, 2001). A relatively flat REE trend for the ash and bentonite shifted, for the Mn pods, to an upward trend with a higher proportion of MREEs and HREEs than LREEs (e.g. the La_{UCC} concentration increased by three times between ash and Mn pods while that of Dy_{UCC} increased by 40 times).

The UCC-normalized trends also showed anomalous Eu and Ce concentrations, where an anomaly was defined as the deviation of the UCC normalized concentration of the element from the mean of the two adjacent elements and is symbolized by REE/REE* (Bau et al., 1996). The Eu/Eu* shows a negative anomaly that remained relatively constant in all samples (Table 1) and constituted an imprint of the rhyolitic source ash (Bau, 1991). Differently, the Ce/Ce* values showed no anomaly in the ash and top bentonite, but a negative anomaly in the lower bentonite and in the Mn pod samples (Table 1); a trend that suggests remobilization of REE during post-depositional processes.

Neodymium, Eu, Dy, Tb, Y, and Er are considered to be critical REEs due to their broad use in current technologies and limited supply. Seredin and Dai (2012) and Dai and Finkelman (2018), drawing on their coal research, proposed to evaluate the economic potential of alternative deposits based on the proportion of critical elements with respect to the total ($REE_{def,rel}$) and the outlook coefficient (C_{out}), which was defined as the ratio between critical REEs and excessive REEs (Ce, Ho, Tm, Yb, Lu). The $REE_{def,rel}$ of the Helms deposit increased from ~30% in the top bentonite and mixed-ash interval to 40% in the lower bentonite and 45% in the Mn pods while the outlook coefficient C_{out} increased from slightly less than 1 to a range of 1.5–2 (Table 1), a range of values that falls into the promising interval of this classification ($30\% < REE_{def,rel} < 51\%, 0.7 < C_{outl} < 1.9$; Supplementary Fig. S2). Accordingly, the Helms bentonite deposit, and especially the Mn pods at its base, have the characteristics of a promising alternative deposit that would expand the use of resources already mined for other purposes (bentonite).

Mineralogy by X-ray Diffraction

The Gonzalez bentonite deposits owe their economic importance to their uniform mineralogy, dominated by either Ca- or Na-saturated montmorillonite (e.g.

Table 1 REE Concentrations (ppm). Samples B13-08 and B13-04 are from the top and bottom bentonites, respectively; V13-01 is from the mixed-ash interval, 13–01 >20 mm coarse size (ash); and Mn14-01 and Mn13-03 are from Mn pods. UCC: Upper Continental Crust model by McLennan (2001). The measured (meas) and certified (cert) values of the SY-4, OREAS, and REE-1 standards that were run with the samples are also reported

	B13-08	V13-01	V13-01, >20 µm	B13-04	Mn14-01	Mn13-03	UCC	SY-4 meas	SY-4 cert	OREAS meas	OREAS cert	REE-1 meas	REE-1 cert
La	65.1	136	74.7	62.1	1030	1300	30	61	58	811	789	1690	1661
Ce	116	301	168	79.9	1730	1280	64	126	122	1360	1331	>3000	3960
Pr	15.4	35.9	18	13	286	301	7.1	15.4	15	128	127	452	435
Nd	54.7	131	64.7	49.4	1180	1260	26	60.4	57	389	378	1520	1456
Sm	10.3	25.2	12.5	10.1	282	302	4.5	12.8	12.7	50	48	401	381
Eu	1.21	3.34	1.62	1.38	42.9	50.4	0.88	1.92	2	7.77	7.77	24.4	23.5
Gd	8.2	17.8	9.4	10.3	290	346	3.8	13.2	14			421	433
Tb	1.3	2.6	1.4	1.7	55.4	59.4	0.64	2.6	2.6	5.2	5.37	113	106
Dy	7.8	13.4	8.5	11.5	390	371	3.5	18.1	18.2	31.5	32.1	893	847
Y	36	50	37	62	1795	1330	22	115	119				
Ho	1.5	2.1	1.6	2.3	80.7	69	0.8	4.2	4.3	6.3	6.34	213	208
Er	4.1	5.7	4.7	6.5	260	193	2.3	14	14.2	28.4	18.7	727	701
Tm	0.58	0.78	0.68	1.01	43	27.5	0.33	2.17	2.3	2.69	2.66	112	106
Yb	3.8	5.1	4.6	6.8	324	183	2.2	14.8	14.8	17.4	17.6	708	678
Lu	0.57	0.78	0.71	1.1	49.3	27.8	0.32	2.2	2.1	2.63	2.58		
ΣREE	326.6	730.7	408.1	319.1	7838.3	7100.1	168.4						
C_{outl}	0.87	0.67	0.68	1.55	1.93	2.28	0.82						
$REY_{def, ref}$	32.19	28.2	28.89	41.52	47.5	45.97	0.33						
Eu/Eu^*	0.62	0.74	0.7	0.64	0.7	0.73	1						
Ce/Ce^*	0.84	0.98	1.04	0.64	0.73	0.47	1						

Springer
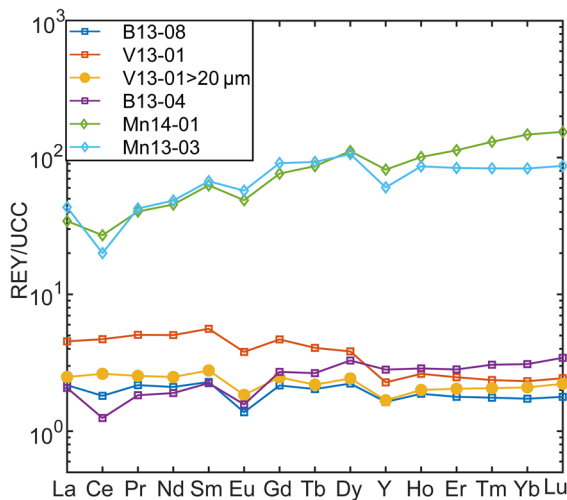
Fig. 2 Helms deposit UCC-normalized REE trend

Berti et al., 2022; Chen, 1968; Chipera & Bish, 2001). The Helms ashfall deposit is composed of Ca-saturated montmorillonite with a variable minor fraction of opal-C. Volcanic glass shards are abundant in the mid-section of the deposit, and a minor fraction of volcanic phenocrysts has been identified that includes sanidine (most abundant), zircon, and titanite.

While the mineralogy of the bentonite is uniform, the XRD patterns showed changes in the Mn

minerals that occur in different pods, despite the short distance between them (Fig. 3). The most abundant manganese mineral identified in sample 13–03 was the hydrated layer-structured ranciéite, which contains Ca as the dominant interlayer cation, and birnessite. In sample 14–01, the mineralogy also included tunnel-structure Mn oxides, primarily todorokite but also hollandite.

Microscale Investigation by SEM

SEM-BSE images were collected from representative Mn pod samples, as well as from the two bentonite intervals and the intervening ash interval; in addition, >250 EDS spectra were collected by point-ID, focusing on regions with high BSE contrast.

The images reveal a severely disrupted clay fabric in the Mn oxide deposits (Fig. 4, Supplementary Fig. S3). The orientation of tightly-packed montmorillonite clay particles changed direction, following the contour of large voids — of the order of tens to hundreds of microns. The void space was occupied partially by a porous network of Mn oxide lamellae forming a cellular fabric (Fig. 4a) having a variable relative porosity, leading to variable BSE contrast in the images (Supplementary Fig. S3). Sheets of Mn-oxides with ranciéite-birnessite composition also grew in face-to-face contact with the montmorillonite (Fig. 4b), frequently
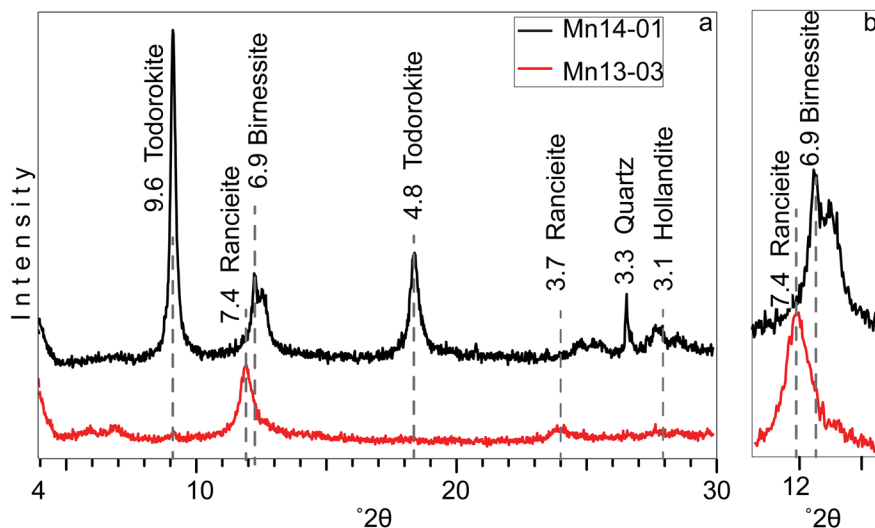
Fig. 3 a XRD patterns of the manganese samples (1–2 μm fractions); b the region around 12°2θ is enlarged x2 to better show the peaks of ranciéite and birnessite
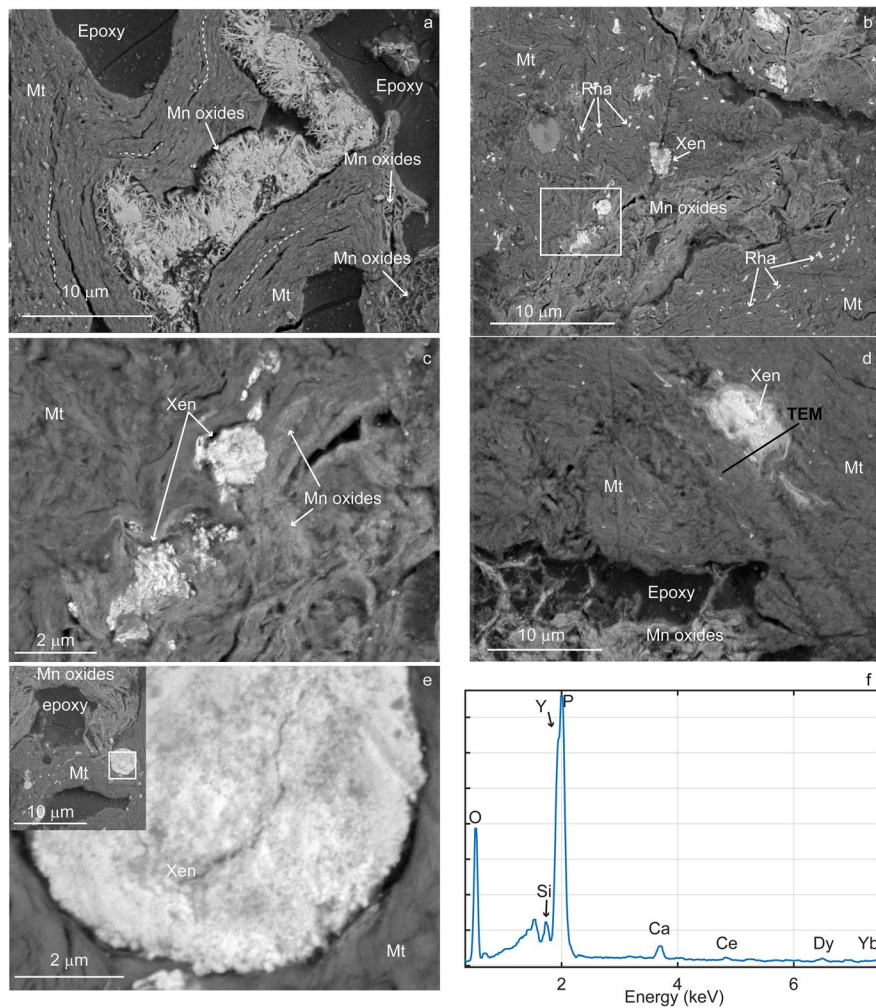
Fig. 4 SEM-BSE images of REEs in Mn pods. **a** Mn oxides framework within montmorillonite (Mnt) void space; the dotted lines mark the orientation of clays. **b** Rhabdophane (Rha) and xenotime (Xen) aggregates dispersed in clay matrix. **c** Region marked by white rectangle in **b** showing xenotime aggregates next to Mn oxides and clays. **d** Xenotime aggregate with boundaries fading into bentonite. **e** Xenotime sub-rounded aggregate in bentonite showing nanoparticle composition; in the inset the lower magnification image shows the location of the aggregate with respect to bentonite and Mn oxides. **f** EDS spectrum from one of the aggregates shows peaks of Y, P, and O with trace concentrations of Ce, Dy, and Yb

bulging the otherwise tightly packed clay fabric. Clay domains, with oriented and tightly packed fabric, changed in orientation and clearly bent around some Mn oxides. Relics of partially altered sanidine and glass shards were also found, plus rare occurrences of zircon and Fe-coated Ti-oxides, as well as rounded quartz grains, within a heterogeneous fabric (at least at the scale of observation of the SEM).

The results of the EDS survey indicated that all the Mn phases contained Ca (the atomic percent ratio of Ca/Mn ranged 0.01–0.2, with a median of 0.05) and Ba (atomic % of Ba/Mn median 0.03; range 0.01–0.07) whereas Fe was detected in only 75% of Mn-phases at low concentrations (atomic % Fe/Mn between 0 and 0.24, median 0.04), in agreement with the bulk analysis findings. Sheet Mn oxides with greater BSE contrast contained Zn (atomic % Zn/Mn of 0–0.15, median 0.04). Less frequently, minor amounts of K, Co, Ni, Cr, Cl, Sr were detected, and, among REEs, Ce was the only element detected in 13% of Mn phases, at low concentrations; however, due to partial overlap with Ba peaks, EDS

may underestimate Ce. Other REEs have only been detected as phosphate nanoparticles with two main groups of compositions: one dominated by LREEs, and a second dominated by Y with small amounts of HREEs (see the correlation matrix heatmap in Supplementary Fig. S4).

Irregularly distributed REE nanoparticles were encountered very frequently in the clay matrix (Fig. 4). In particular, the Y-phosphate nanoparticles, composed of xenotime (see TEM section), formed agglomerates ranging between 2 and 7 μm in diameter that are distinctive of these Mn pods (Fig. 4c–e). Some agglomerates show well defined boundaries while others showed halos at the transition to clay or appear smeared (Fig. 4d) or continue into narrow voids linking them to other agglomerates. SEM images acquired at high magnification clearly showed tightly packed nanoparticles composing the agglomerate (Fig. 4e), whereas EDS spectra (Fig. 4f) consistently showed peaks of O, Y, and P, and trace amounts of Ca, Ce, Dy, and Yb, as well as other heavy REE that were not always detected as their peak intensity was near the detection limit of the EDS. Even though Y and P peaks partially overlapped in EDS spectra, their presence was evident from the resultant compounded peak shape with two separate maxima, which was decomposed using the software *AZtec®*. Analysis by TEM-EDS (see TEM section) further confirmed the presence of the YKα peak at 14.93 keV.

Other nanosize phosphates that hosted mainly light REEs were also frequent in the Mn pods, clustered in small aggregates, and having a larger mean particle size than the xenotime (Fig. 4b, Fig. 5a). The EDS data collected from these LREE-phosphate that were identified as rhabdophane by TEM analysis (see TEM section) indicated changing relative proportions of REEs between aggregates, particularly with respect to Ce (Fig. 5b). For a more quantitative estimate of REE variation in rhabdophane, the wt.% ratio of Ce and Nd with La was calculated (these REEs are usually present in rhabdophane and their peaks are little affected by overlaps) of different aggregates in the Mn pods, which resulted in means with standard deviation values of 0.42 ± 0.3 and 1.13 ± 0.15 for Ce/La and Nd/La, respectively. The large standard deviation confirmed the dramatic variability in the proportion of Ce. Rhabdophane in the Mn pods also hosted Y in sufficient concentration

to cause an asymmetry on the left side of the P peak (confirmed by TEM), indicating a mean wt.% Y/La ratio of 0.83 ± 0.19, and trace amounts of S.

Such variability is in stark contrast with the uniform composition of LREE-phosphates found in the ashfall deposit sediments where it is uninfluenced by Mn oxides. Though fewer EDS spectra were collected from the bentonite and ash-bentonite mixed intervals, they all showed uniform intensity profiles and minor changes in the proportions of REEs, as indicated by mean Ce/La and Nd/La wt.% ratios of 1.47 ± 0.12 and 0.827 ± 0.06. Yttrium, identified by Lα peak corresponding to 1.92 keV, resulted in a Y/La mean wt.% ratio of 0.54 ± 0.07; Th and U were present at concentrations close to the detection limit (Fig. 5d).

The morphology and texture of LREE-phosphates also differed between the Mn pods and the ashfall deposit. LREE-phosphates in the Mn pods have rod-shaped morphology with edges at 90° angles, whereas in the ashfall deposits LREE-phosphates are smaller and have flaky morphology similar to that of clay particles. In fact, TEM analysis of flaky LREE-phosphates in a white bentonite from the nearby H. W. Johnson pit — which formed by alteration of the same ash layer (Yancey et al., 2018) — were identified as monazite, an anhydrous REE-phosphate mineral (Berti et al., 2022). These differences suggest that interaction with pore fluid drove dissolution in the ashfall deposit and reprecipitation in the Mn pods.

TEM

Further details were attained from TEM analysis of a FIB section extracted from a Y-phosphate mass surrounded by clay, which occurred near a vein filled with Mn oxides (Fig. 6a). The TEM-HAADF imagery, where contrast is proportional to atomic number, revealed this mass had a complex texture (Fig. 6b–d) with a band of loosely arranged nanoparticles on the right, a central region with the morphology of a single grain, and a scalloped texture on the left. In spite of its single grain appearance, higher magnification TEM images of the central and left regions showed a mottled texture arising from changes in diffraction contrast (Fig. 6d). Most importantly, SAED patterns (Fig. 6e) collected from ~200 nm diameter circular areas at different locations showed clear broad spotty rings that
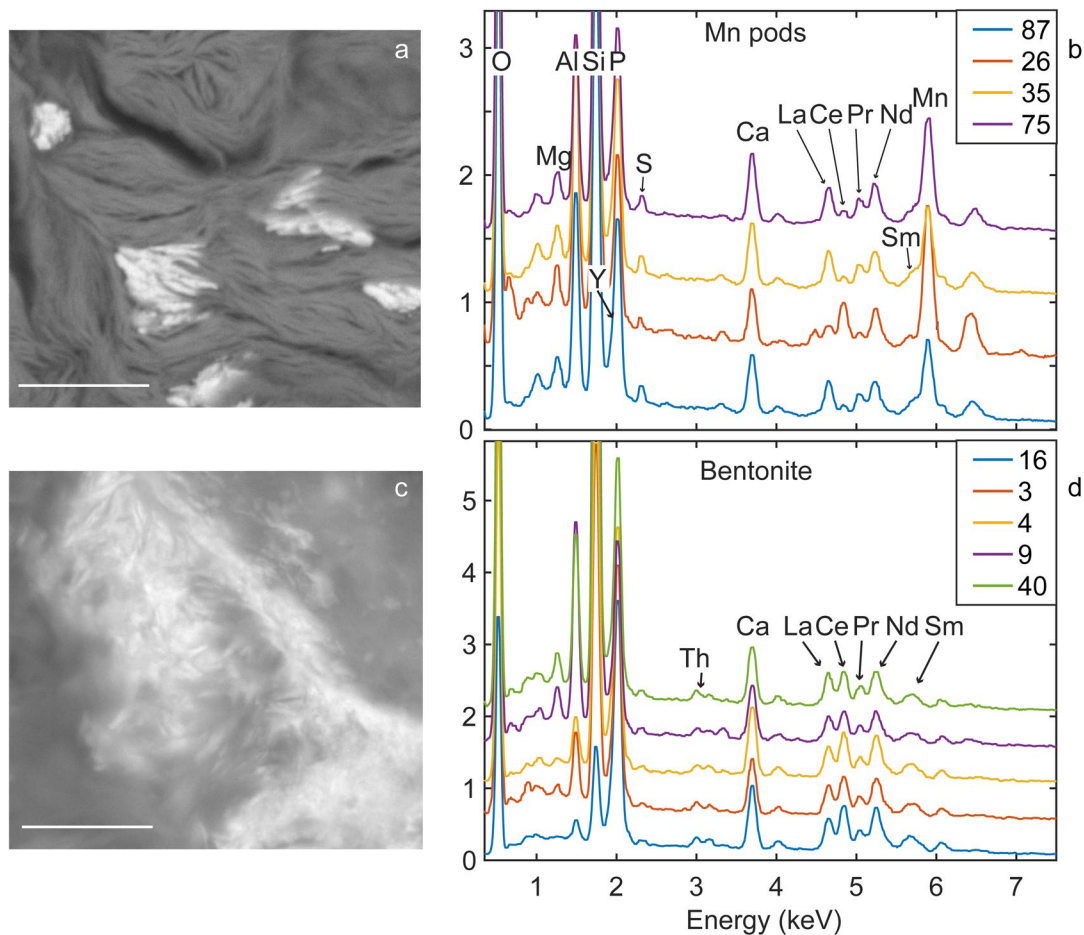
Fig. 5 Comparison of EDS spectra of LREE-phosphates in Mn pods and ashfall deposit. **a** BSE Image of rhabdophane particles in Mn pods. **b** EDS spectra collected from different aggregates in the Mn pods. **c** BSE image of LREE-phosphate in bentonite interval. **d** EDS spectra from different aggregates in the bentonite interval. Scale bar in **a** and **b** is 1 µm

are evidence of diffraction from multiple crystals while the nanosize of the crystals contributed to the broadening of the rings. Comparisons of the SAED intensity profiles of three selected areas (Fig. 6b) are indicated by red circles 6, 8, 9, where the profiles were extracted around a radius vector k, with length of 10 nm^{-1} (k = 1/d-space), rotationally averaged between 0 and 360^0. All the profiles were similar (Fig. 6f), displaying peaks at the same **k** positions and relative intensities that matched those of xenotime, assuming random orientation and the structure of Ni et al. (1995).

The EDS spectra collected by point ID and by mapping the bottom region of the grain (Fig. 6, Supplementary Fig. S5) confirmed the composition of Y phosphate in all regions of the aggregate, with trace

amounts of Ca, Ce, Dy, and Yb. Because Dy and Fe peaks partially overlap, broad Fe peaks implied the presence of Dy, and this was verified when the two peaks were resolved by decomposition using *AZtec®* software. The EDS did not detect changes between regions with different texture, except for lower signal intensity from the scalloped region which was due to greater porosity and lesser section thickness.

The TEM and HRTEM images collected from the central region, the scalloped region, and the transition between them showed the presence of crystals mainly in the size range between 20 and 60 nm, with fewer crystals in the size range 100–150 nm (Fig. 7). Changes in the direction of lattice planes at crystal boundaries (Fig. 7b, d), as well as crystal strain from misfit from crystal defects, caused the contrast
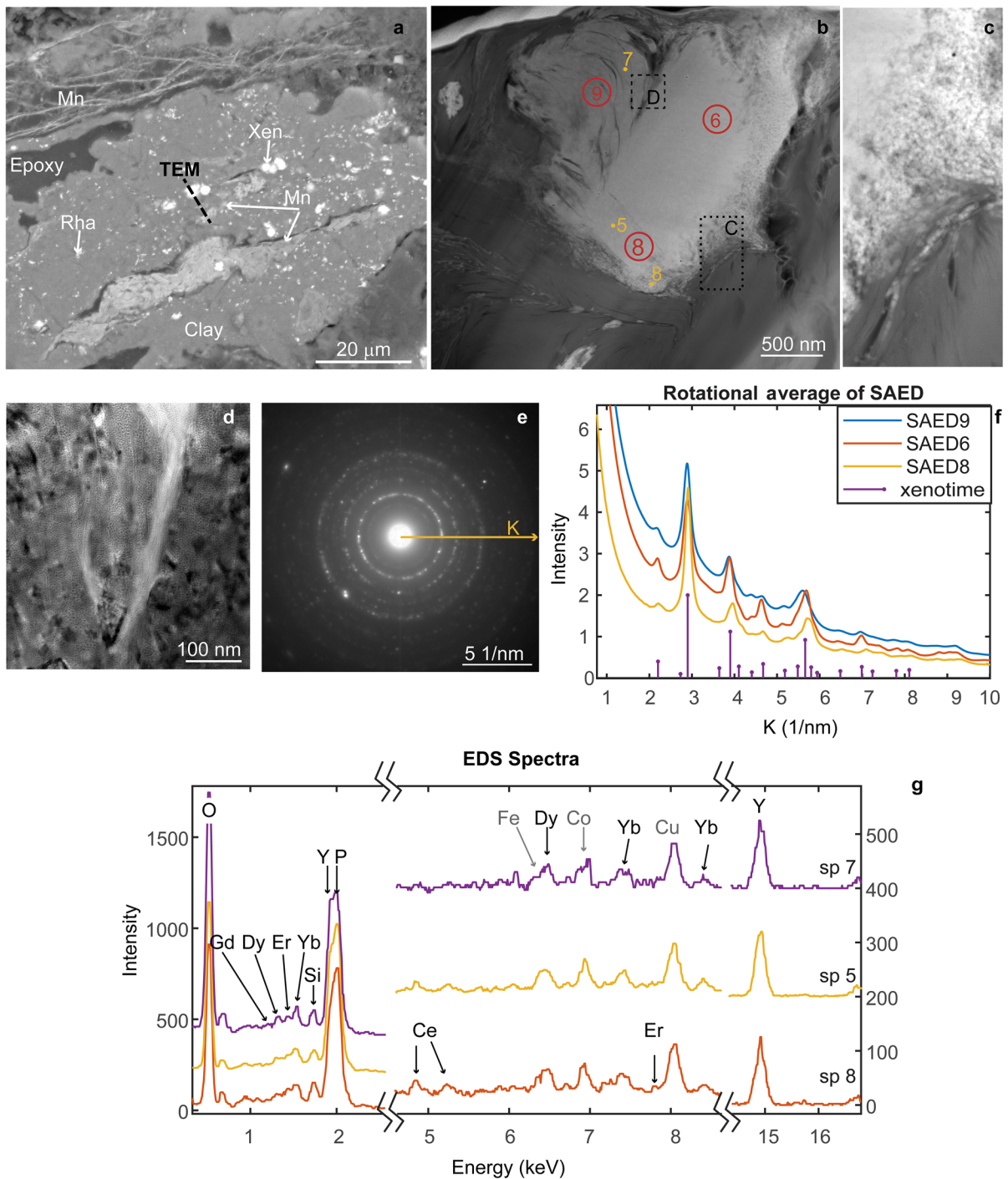
Fig. 6 FIB section from xenotime. **a** SEM-BSE image with location of the FIB section marked. **b** TEM-HAADF image of the FIB section where numbered points mark the locations of EDS while the red circles show the SAED patterns. **c** Higher magnification HAADF from location marked by black dotted rectangle in **b**. **d** TEM image of the area marked by the dashed rectangle in **b**. **e** Example of SAED pattern from the aggregate showing a ring pattern. **f** Rotational average intensity profiles calculated from SAED patterns collected from the areas marked 6, 8, 9 in **b**, and simulated K positions and relative intensities of xenotime according to the structure of Ni et al. (1995). **g** Three stacked TEM-EDS spectra of xenotime, collected from locations marked by dots 5, 7, 8 in **b**. The x-axis of the plot has been split into three regions to show the peaks from the main elements (O, P, and Y), plus elements occurring in trace amount (Ce, Dy, Er, and Yb); Fe, Co, and Cu peaks are from the instrument and TEM grid

changes that confer a mottled texture to the TEM images.

The multi-grain xenotime is enveloped by domains of tightly packed montmorillonite layers in face-to-face contact (visible as lines in Fig. 6a); the domains change orientation so as to follow the contour of the xenotime. In Fig. 8, the HAADF-TEM image shows that sheets of Mn oxide (bright contrast) arranged in face-to-face contact with the clays fill the void space in between clay domains and seem to grow laterally. EDS spectra collected from several bright contrast particles determined that the sheet particles are Mn oxides with Ca and Ba or Ca and Zn. While REEs were not detected by TEM-EDS in the Mn oxide minerals, particles

of xenotime and rhabdophane were identified next to them (Fig. 8).

Light REEs were identified in rhabdophane ($REEPO_4 \bullet 1.5H_2O$) nanoparticles that form smaller aggregates than xenotime, their presence bending the surrounding clays (Fig. 9). The HRTEM images and SAED patterns show a lattice with hexagonal symmetry, i.e. lattice planes at 60° angles in the HRTEM image (Fig. 9b) and equidistant reflections at 60° in the SAED. This symmetry combined with a lattice d spacing of 6.1 Å match well with the rhabdophane structure (Mooney, 1948), viewed along [001]. While the TEM image clearly showed multiple particles, the symmetric SAED pattern resembled a single crystal, except
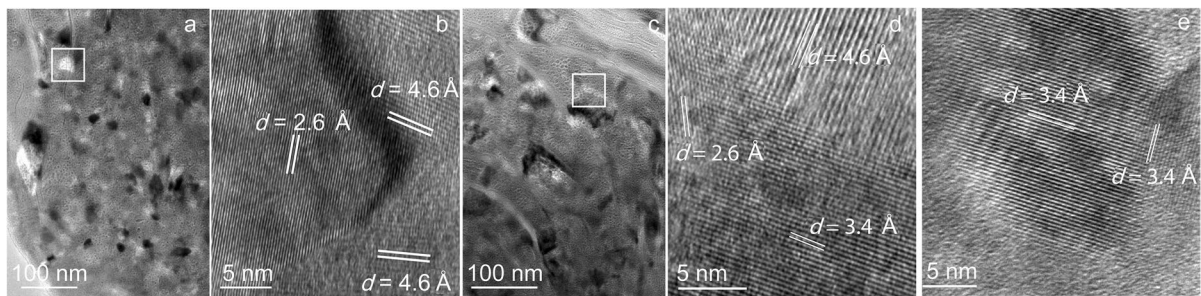

Fig. 7 High-resolution TEM images from the aggregate. **a** Dense region showing variations in contrast due to multiple crystals; the white square marks the location of the HRTEM in **b**. **b** Strain at crystal boundaries due to change in lattice orientation appear dark. **c** Scalloped texture where bending arises from gradual change in crystal orientation, the white rectangle marks the location of **d**. **d** Lattice planes with different orientations at boundaries. **e** Nanoparticles as small as 20 nm attached by an edge
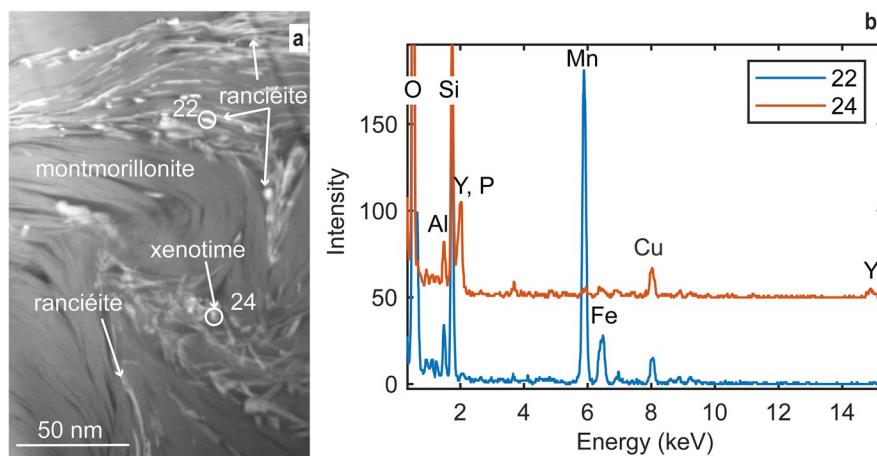
Fig. 8 HAADF TEM image and corresponding EDS spectra of Mn oxides and xenotime growing between clays. **a** Bright contrast platy or prismatic particles of Mn oxides (ranciéite) and rare xenotime nanoparticles. **b** EDS spectra collected from the numbered circles in **a**. Note: Cu peak is from the grid
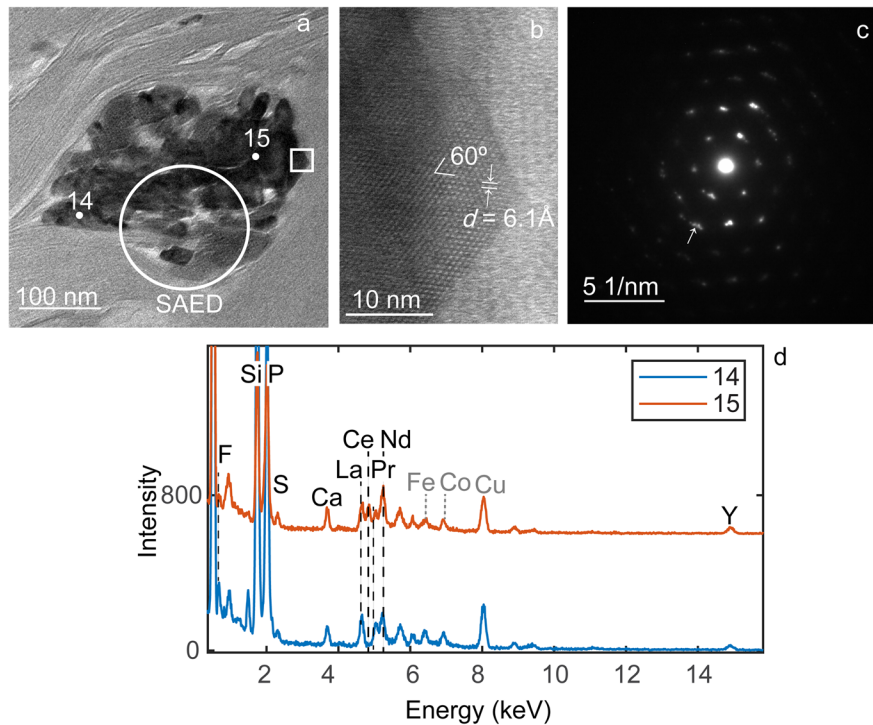
Fig. 9 TEM of rhabdophane. **a** TEM image of aggregate of rhabdophane nanoparticles (dark contrast) in clays. **b** HRTEM from square region in **a** shows a hexagonal lattice with d-spacing of 6.1 Å. **c** SAED from the circle region in **a**; the arrows indicate where multiple spots are visible. **d** EDS spectra from points 14 and 15 in **a**. Note: Cu, Fe, and Co peaks are from the grid and instrument, not the sample

for peak broadening, striking, and fragmentation (see arrows in Fig. 9c) that denote an assembly of iso-oriented nanocrystals. The EDS spectra collected from two points in the aggregate (marked 14 and 15 in Fig. 9a) indicate a composition of phosphate with light REEs, Y, and trace amounts of S and F (Fig. 9d). Notably, the proportions of Ce relative to other REEs change within the aggregate, and similar variability was found in other aggregates analyzed by TEM as well. Silicon and Al are from the clay rather than phosphate. Similar results were obtained from TEM analysis of a second FIB lift-out section from the location marked in (Fig. 4d).

Discussion

Rhyolitic ash beds provide a source of REEs for the Eocene Texas deposits that can be remobilized by alteration of the ash into bentonite (Badurina & Šegvić, 2022; Berti et al., 2022; Zielinski, 1982), but also by successive episodes of fluid migration

and invasion. The Helms deposit shows complex changes in the REE trend (normalized to UCC), as the relatively flat REE trend of the ash fraction changed to a LREE enriched trend in the mid-section and top bentonite (Fig. 2), a change that has also been observed in other bentonite deposits in Gonzales, Texas (Michaedilis, 2011; Heintz et al., 2015) and elsewhere (Badurina & Šegvić, 2022). In the lower bentonite, however, the UCC-normalized trend shows M, HREE enrichment, as well as a negative Ce/Ce*. Remarkably, in the Mn pods the M, HREE enrichment was amplified with respect to the lower bentonite while the negative Ce anomaly was retained, accompanied by an order of magnitude higher REE enrichment. These variations across the deposit are consistent with the type of fractionation resulting from transport in solution (Bao & Zhao, 2008; Li et al., 2020; Migdisov et al., 2016; Nesbitt, 1979;) where fractionation between the light, medium, and heavy REE results from the REE tendency to form different secondary minerals,

complexes with different ligands in solutions, or different reactivity with particulate surfaces (Nesbitt, 1979; Johannesson et al., 1996; Censi, 2007). Further, the negative Ce/Ce* that developed in the lower bentonite and Mn oxides indicates precipitation from a solution depleted in Ce by oxidative scavenging, possibly catalyzed by adsorption on the surface of Mn oxides.

Alteration of volcanic ash into bentonite is accompanied by a loss of permeability (Galloway, 1978) as bentonite is impermeable; however, at the Helms pit, the development of sets of fractures cutting across bedding allowed for pore water from the overlying sand layer to percolate down. Additionally, the sharp boundaries between sandstone and bentonite function as discontinuities along which pore water can migrate laterally. Excavation exposures at the pit showed that Fe (oxyhydr) oxides deposited preferentially on fracture walls at the top and mid-section of the bentonite, whereas Mn oxide crusts precipitated at layer interfaces and Mn pods formed at the base of the ashfall deposit (Fig. 1). This zonation between Fe and Mn (oxyhydr)oxides indicates oxidizing conditions and downward flow direction of the fluid from which they precipitated because of the faster kinetics of Fe oxidation which requires a less oxidizing environment and lower pH than Mn, due to different reaction pathways (Liu et al., 2022; Luther, 2005). Fractures terminate at the base of the bentonite, in correspondence with the boundary of a cemented sandstone. At the junction between fracture termination and layer boundary, invasion of the bentonite by the percolating fluid is evidenced, at the micro-scale, by the disturbed fabric of the clay, the tremendous expansion of void space, and the presence of authigenic Mn oxides and rare earth phosphates which bent and displaced surrounding clays (Fig. 4). Once precipitation began at one junction, Mn oxides continued to grow for as long as leaching through fractures persisted, thus growing into pod-shaped deposits that eventually bulged the overlying bentonite layers (Fig. 1). Lateral flow at the clay-sandstone boundary, favored by a gentle dip, may have accompanied the growth of the pods, thus contributing to the formation of veins and crusts. At the outcrop scale, this process resulted in a patchy distribution of Mn oxides pods including REEs.

The source of the Fe and Mn dissolved in the water percolating through the fractures is uncertain. In contrast to other major elements (e.g. Si, Al), the behavior of Mn during alteration of volcanic ash is more variable. For instance, Zielinski (1982) reported an increase in Mn concentration from volcanic ash to bentonite in the Troublesome Fm (Kremmling, Colorado) that he attributed to either structural incorporation in the clay structure or precipitation of hydrous secondary oxides. Namayandeh et al. (2020) reported both depletion and enrichment of Mn in Iranian bentonite deposits relative to their parent ash, while Christidis (1998) reported no change but negligible Mn concentrations between ash and bentonite in deposits of the Aegean islands (Greece). In the Helms deposit, the very low Mn concentration (~0.06%) does not change in the mid-section between clay and ash fraction. Although the Mn concentration decreases in the top and bottom bentonite intervals (Table S1) suggesting some removal from the system, the amount released was minimal; additionally, the concentration of Fe is low (~1%) and uniform within the deposit (Table S1). Therefore, it was inferred that Fe and Mn were transported in pore fluid that migrated laterally in the sand layer on top of the bentonite or at the boundary in between the two — possibly following the groundwater path for long distances — before reaching the fractured section of the ashfall deposit where fluid percolation through the fracture system drove alteration of glass shards (which released REEs) as well as authigenic REE nanominerals.

The anomalously high concentrations of some metal ions in the pods, compared to UCC, derived from the strong adsorption and incorporation capacity that Mn oxides have for metal ions. Such enrichments are a common feature of ferro-manganese chemical deposits found at the bottoms of oceans, seas, lakes, rivers, and in the sedimentary record; their composition is widely used as a geochemical proxy (e.g. Bau et al., 2014; Liu et al., 2022; McKenzie, 1989). Marine ferromanganese deposits are classified based on the type of fluid from which they precipitated as hydrogenetic (from seawater), diagenetic (from pore water), and hydrothermal — each type being characterized by a different chemical signature (e.g. Bau et al., 2014; Bonatti et al., 1972; Conrad et al., 2017). While geological evidence indicates that Mn pod formation is more recent than the deposition

of the Helms ash layer and its alteration into benton-ite, the data collected in this study were not sufficient to establish whether the formation of the Mn pods occurred in the presence of saline fluids in water where the ash was deposited or in the presence of low salinity water after the sediment was exposed on the coastal plain and subjected to groundwater flow conditions. Keeping in mind such limitation, the Helms Mn pods have a composition consistent with a diagenetic origin, for the lower concentrations of Co, Ni, and Cu than hydrogenetic deposits and higher Mn/Fe than hydrogenetic and hydrothermal deposits (Bonatti et al., 1972; Conrad et al., 2017; Sasmaz et al., 2020, 2021). Hydrothermal origin is further excluded by the geology of the region. Additionally, the normalized REE trend of marine diagenetic Mn oxides — inherited from seawater — is also similar to that of the Helms Mn oxides, especially the negative Ce/Ce* which in seawater derives from oxidative scavenging catalyzed by particulate surfaces (Bau et al., 1996, 2014; Sasmaz et al., 2020, 2021). However, the concentration of REEs is higher than what was reported for most other Fe–Mn deposits. For example, from a review of marine Fe–Mn deposits Bau et al., 2014 reported maximum total REE concentrations of 2282 ppm, and a median value for diagenetic nodules of 349 ppm; Conrad et al. (2017) reported total REE of ~2250 ppm from the California continental margin; Sasmaz et al. (2021) reported a mean total REE of 199 ppm for the Mn oxides sedimentary deposits of Chiatura, Georgia; and a mean total REE of 108 ppm for those of Nikopol (Sasmaz et al., 2020). The higher concentration in the Helms Mn pods (> 7000 ppm) supports weathering of the ashfall bed as the main REE source rather than adsorption from seawater.

The investigation by SEM and TEM of the rare earth occurrences added a better understanding of the remobilization processes that shaped these deposits. Whereas rare nanoparticles of xenotime and rhabdophane are found associated with thin sheets of ranciéite in the interlayer space of montmorillonite (Fig. 8), they are far more commonly separated from the Mn oxides in mineralogically segregated aggregates, suggesting a tendency of REE complexes to infiltrate farther into the ultrafine pore space of the montmorillonite than Mn. Nonetheless, the association indicates co-precipitation from the same aqueous solution under oxidizing conditions

and that these authigenic minerals did not form by desorption of REEs during reductive dissolution of Mn oxide particulates (e.g. Och et al., 2014; Sasmaz et al., 2020).

The xenotime aggregates of the Helms Mn pods are remarkable for their texture, morphology, and composition (Fig. 4, Fig. 6) which are consistent with rapid, heterogeneous nucleation from a supersaturated, percolating aqueous solution. Formation of xenotime has been reported in a broad range of geologic settings. In sedimentary and especially coastal settings, xenotime is usually found as epitaxial overgrowth on zircon, with which it is isostructural (Drost et al., 2012; Hay et al., 2009; Rasmussen, 2005; Rasmussen et al., 1998). Similar overgrowths were observed in the Helms bentonite (current study) and in the nearby bentonite deposit at the H.W. Johnson pit (Berti et al., 2022) but zircon is not associated with the xenotime aggregates in the Mn pods. Even for aggregates comprising a dense core surrounded by a halo or seemingly overgrowth, high resolution SEM and TEM images showed clearly that both the core and the halo/overgrowth regions are composed of nanoparticles, more and less densely packed, respectively (Fig. 6, Fig. 7), while EDS and SAED showed composition of xenotime; therefore, the different textures of the xenotime indicated different conditions of growth.

It seems unlikely that the xenotime core is a pseudomorph of a zircon grain which served as a substrate for epitaxial growth of the outer xenotime regions, and subsequently underwent complete dissolution and replacement because the concentration of Zr remained unchanged from the ashfall deposit (~130 ppm, as measured by ICP-MS). Further, zircon solubility is extremely low, and even in reported cases of (metamict) zircon dissolution by alkaline fluids at ambient temperature, re-precipitation occurs right on the grain rim or within a few microns (Delattre et al., 2007; Franz et al., 2015; Hay et al., 2009). It is also unlikely that the xenotime nanocrystals replaced a xenotime phenocryst that sourced the Y and P during congruent dissolution, as the solubility of xenotime phenocrysts is very low (Budzyń & Sláma, 2019; Cetiner et al., 2005), and the ICP-MS data indicated that Y was transported to the pods, along with the other REEs. Hence, it is more plausible that the xenotime aggregates (including their dense core) formed by

precipitation from a supersaturated solution via heterogeneous nucleation when the solution flow became restricted by the narrowing of pore sizes, as it invaded the montmorillonite. Like epitaxial growth on zircon, fluid supersaturation would effectively lower the free-energy barrier to nucleation (De Yoreo et al., 2015), yielding crystalline nanoparticles as small as 20 nm with poorly defined habit. Within densely packed cores like the one shown in Fig. 6, competing processes of coalescing nanoparticles and crystal growth are suggested by the large number of crystal defects and by some larger crystals (hundreds of nanometer range) with the di-pyramidal habit typical of xenotime, respectively (Fig. 7). A prolonged period of solution percolation along the same pore conduits would support aggregate growth, while also expanding the pore space, thereby modifying the flow path and velocity around the aggregate. Consistent with this interpretation, shadowing from the aggregate in Fig. 6, indicates a region of slower flow that allowed growth of larger crystals, elongated along the flow direction, which merged into a scalloped texture.

The crystal chemistry of xenotime remains rather uniform within the aggregate and between aggregates as demonstrated by the TEM-EDS and SEM–EDS data, respectively. Trace amounts of Dy, Yb, and other MREEs and HREEs in xenotime (Fig. 4,Fig. 6g) are common because their ionic radius — ranging between 0.97 and 1.04 Å (Clavier et al., 2011) — is similar to that of Y and, thus, favors isomorphous substitutions. Peak overlap and low concentrations limit the applicability of EDS-based quantification; nonetheless, at first approximation, a comparison between wt.% ratios calculated based on TEM-EDS for xenotime and ICP-MS for the same bulk sample showed similar ratios for Dy/Y (0.18 and 0.22), Ho/Y (0.03 and 0.04), and Yb/Y (0.21 and 0.18); other MREEs and HREEs are either at too low concentration or are more affected by peak overlapping to consider. Therefore, in principle, xenotime precipitation has the potential to affect the bulk concentration of MREEs and HREEs in the sample. Nonetheless, additional occurrences of MREEs and HREEs as absorbed ions on Mn oxides, or as exchangeable ions in the clays at concentrations below the EDS detection limit, are possible.

The persistent, small amounts of Ce in the xenotime are less straightforward to explain by isomorphous substitutions given the large difference in ionic radius between Ce^{3+} and Y. In fact, Ce (like the other LREEs) is commonly below the EDS detection limit in primary xenotime (Clavier et al., 2011) or even in xenotime overgrowths on zircon found in hydrothermal or diagenetic environments which tend to have a more complex composition (Drost et al., 2013; Franz et al., 2015). One possible explanation is that xenotime is hosting Ce^{4+} (its ionic radius being similar to that of Y) which implies that Ce oxidation was ongoing during precipitation of xenotime and Ce^{4+} was scavenged by xenotime. Substitutions of tetravalent cations have been reported in xenotime (and other REE phosphates); in fact, Zr, which is also tetravalent, was also detected in the xenotime. Charge balance was restored by coupled substitutions with divalent cations, in this case Ca^{2+} (Clavier et al., 2011). Accordingly, an approximate formula for xenotime can be estimated from quantification of the TEM-EDS data using the Cliff-Lorimer method (Cliff & Lorimer, 1975): $Y_{0.67}Ca_{0.07}Zr_{0.02}Ce_{0.04}Gd_{0.02}Dy_{0.06}Ho_{0.01}Er_{0.03}Yb_{0.07}U_{0.01}PO_4$.

Some adsorption of Ce on Mn oxides is indicated by the EDS data; however, the rarity of Ce detection in Mn oxides and the negative Ce/Ce* detected in the Mn pods indicate that this process is minor in the pods. Rather, the Ce/Ce* trend within the ashfall deposit (Table 1, Fig. 2) suggests that Ce precipitated shortly after remobilization and perhaps is present in larger concentrations than other LREEs in Mn oxide veins closer to the mid-section of the ashfall deposit or in Fe (oxyhydr)oxides crusts that coat fractures across the lower bentonite.

It is noteworthy that Ce is decoupled from other light REEs also in the rhabdophane — the main phase hosting LREEs in the Mn pods. TEM-EDS analysis demonstrated dramatic changes in Ce concentrations even within the same nanoparticle aggregate. This compositional variation corroborates rapid precipitation of rhabdophane from a supersaturated solution and is also consistent with experimental studies on crystallization of rhabdophane (Poitrasson et al., 2004; Shelyug et al., 2018). Further, the compositional variability supports the notion that Ce oxidation is ongoing during formation of these secondary phases.

The results suggest other additional interesting aspects of LREE-phosphate formation. The porosity of the rhabdophane oriented aggregates identified by TEM (Fig. 9) may facilitate continuation of the

interaction with circulating pore fluid, resulting in more compositional changes as they develop. Also, the stark changes that were identified between the LREE-phosphates in the Mn pods and those in the bentonite and ash intervals (Fig. 5) suggest different kinetics between the REE phosphates that crystallize during the alteration of volcanic ash into bentonite and the rhabdophane nanominerals that precipitate from the fluid percolating through fractures.

Conclusions

This study utilized SEM and TEM, in combination with EDS, to investigate the modes of occurrence of REEs in Mn oxide-rich pods located at the base of a 4 m bentonite-altered ash deposit, exposed at the Helms pit in Gonzales (Texas, USA), that is partially altered into bentonite. Enrichment of REEs in the deposit ranges between 300 and 730 ppm but increases sharply in the Mn-pods to a maximum of 7800 ppm. This change is accompanied by an increase in proportions of MREEs and HREEs relative to LREEs.

The SEM and TEM results show that nanoparticle aggregates of xenotime and rhabdophane are the main hosts of REEs in the Mn pods. The characteristics of the xenotime and rhabdophane indicate that they formed in a low temperature, weathering environment by rapid precipitation from oxidizing pore fluids within the altered ash deposit. Spatial changes in REE abundances are consistent with downward fluid flow through fractures in the deposit. While Mn also precipitated from these oxidizing fluids, the results suggest a more distal source for the Mn. At the base of the bentonite-altered ash, cemented sandstone prevented further downward flow, prompting lateral invasion of fluids from fractures into the surrounding bentonite, at the sandstone interface, creating conditions for precipitation of both Mn oxides and REE-phosphates. The conditions that induced remobilization in the Helms bentonite deposit are likely to occur in other similar deposits of the Eocene Texas coastal plains and elsewhere, with possibly even greater enrichment. Therefore, the potential of bentonite deposits as a low environmental impact REE alternative source should be explored further.

Declarations

References

Badurina, L., & Šegvić, B. (2022). Assessing trace-element mobility during alteration of rhyolite tephra from the Dinaride Lake System using glass-phase and clay-separate laser ablation inductively coupled plasma mass spectrometry. *Clay Minerals, 57*(1), 1–6.

Bao, Z., & Zhao, Z. (2008). Geochemistry of mineralization with exchangeable REY in the weathering crusts of granitic rocks in South China. *Ore Geology Reviews, 33*, 519–535. https://doi.org/10.1016/j.oregeorev.2007.03.005

Bau, M. (1991). Rare-earth element mobility during hydrothermal and metamorphic fluid-rock interaction and the significance of the oxidation state of europium. *Chemical Geology, 93*, 219–230. https://doi.org/10.1016/0009-2541(91)90115-8

Bau, M., & Koschinsky, A. (2009). Oxidative scavenging of cerium on hydrous Fe oxide: Evidence from the distribution of rare earth elements and yttrium between Fe oxides and Mn oxides in hydrogenetic ferromanganese crusts. *Geochemical Journal, 43*(1), 37–47. https://doi.org/10.2343/geochemj.1.0005

Bau, M., Koschinsky, A., Dulski, P., & Hein, J. R. (1996). Comparison of the partitioning behaviours of yttrium, rare earth elements, and titanium between hydrogenetic marine ferromanganese crusts and seawater. *Geochimica Et Cosmochimica Acta, 60*, 1709–1725. https://doi.org/10.1016/0016-7037(96)00063-4

Bau, M., Schmidt, K., Koschinsky, A., Hein, J., Kuhn, T., & Usui, A. (2014). Discriminating between different genetic types of marine ferro-manganese crusts and nodules based on rare earth elements and yttrium. *Chemical Geology, 381*, 1–9. https://doi.org/10.1016/j.chemgeo.2014.05.004

Berti, D., Slowey, N. C., Yancey, T. E., & Deng, Y. (2022). Rare earth nanominerals in bentonite deposits of the Eocene Texas coastal plains. *Applied Clay Science, 216*, 106373. https://doi.org/10.1016/j.clay.2021.106373

Bonatti, E., Kraemer, T., & Rydell, H. (1972). Classification and genesis of submarine iron-manganese deposits. In D. R. Horn (Ed.), *Ferromanganese deposits on the ocean floor* (pp. 149–166). National Science Foundation.

Budzyń, B., & Sláma, J. (2019). Partial resetting of U-Pb ages during experimental fluid-induced re-equilibration of

xenotime. *Lithos, 346–347*, 105163. https://doi.org/10.1016/j.lithos.2019.105163

Cao, X., Chen, Y., Wang, X., & Deng, X. (2001). Effects of redox potential and pH value on the release of rare earth elements from soil. *Chemosphere, 44*, 655–661. https://doi.org/10.1016/s0045-6535(00)00492-6

Censi, P., Sprovieri, M., Larocca, D., Aricò, P., Saiano, F., Mazzola, S., & Ferla, P. (2007). Alteration effects of volcanic ash in seawater: Anomalous Y/Ho ratios in coastal waters of the Central Mediterranean sea. *Geochimica Et Cosmochimica Acta, 71*(22), 5405–5422. https://doi.org/10.1016/j.gca.2007.09.015

Cetiner, Z. S., Wood, S. A., & Gammons, C. H. (2005). The aqueous geochemistry of the rare earth elements. Part XIV. The solubility of rare earth element phosphates from 23 to 150. *Chemical Geology, 217*, 147–169. https://doi.org/10.1016/j.chemgeo.2005.01.001

Chen, P. Y. (1968) Geology and mineralogy of the white bentonite beds of Gonzales County, Texas. Ph.D. dissertation, University of Texas, Austin, Texas.

Cheshire, M. C., Bish, D. L., Cahill, J. F., Kertesz, V., & Stack, A. G. (2018). Geochemical evidence for rare-earth element mobilization during kaolin diagenesis. *ACS Earth and Space Chemistry, 2*(5), 506–520. https://doi.org/10.1021/acsearthspacechem.7b00124

Chipera, S. J., & Bish, D. L. (2001). Baseline Studies of the Clay Minerals Society Source Clays: Powder X-ray Diffraction Analyses. *Clays and Clay Minerals, 49*, 398–409. https://doi.org/10.1346/ccmn.2001.0490507

Christidis, G. E. (1998). Comparative study of the mobility of major and trace elements during alteration of an andesite and a rhyolite to bentonite, in the islands of Milos and Kimolos, Aegean, Greece. *Clays and Clay Minerals, 46*, 379–399. https://doi.org/10.1346/CCMN.1998.0460403

Clavier, N., Podor, R., & Dacheux, N. (2011). Crystal chemistry of the monazite structure. *Journal of the European Ceramic Society, 31*, 941–976. https://doi.org/10.1016/j.jeurceramsoc.2010.12.019

Cliff, G., & Lorimer, G. W. (1975). The quantitative analysis of thin specimens. *Journal of Microscopy, 103*, 203–207. https://doi.org/10.1111/j.1365-2818.1975.tb03895.x

Conrad, T., Hein, J. R., Paytan, A., & Clague, D. A. (2017). Formation of Fe-Mn crusts within a continental margin environment. *Ore Geology Reviews, 87*, 25–40. https://doi.org/10.1016/j.oregeorev.2016.09.010

Dai, S., & Finkelman, R. B. (2018). Coal as a promising source of critical elements: Progress and future prospects. *International Journal of Coal Geology, 186*, 155–164. https://doi.org/10.1016/j.coal.2017.06.005

Dai, S., Ward, C. R., Graham, I. T., French, D., Hower, J. C., Zhao, L., & Wang, X. (2017). Altered volcanic ashes in coal and coal-bearing sequences: A review of their nature and significance. *Earth-Science Reviews, 175*, 44–74. https://doi.org/10.1016/j.earscirev.2017.10.005

De Yoreo, J. J., Gilbert, P. U. P. A., Sommerdijk, N. A. J. M., Penn, R. L., Whitelam, S., Joester, D., Zhang, H., Rimer, J. D., Navrotsky, A., Banfield, J. F., Wallace, A. F., Michel, F. M., Meldrum, F. C., Cölfen, H., & Dove, P. M. (2015). Crystallization by particle attachment in synthetic, biogenic, and geologic environments. *Science, 349*(6247), aaa6760. https://doi.org/10.1126/science.aaa6760

Delattre, S., Utsunomiya, S., Ewing, R. C., Boeglin, J.-L., Braun, J.-J., Balan, E., & Calas, G. (2007). Dissolution of radiation-damaged zircon in lateritic soils. *American Mineralogist, 92*, 1978–1989.

Deng, Y., White, G. N., & Dixon, J. B. (2013). *Soil mineralogy laboratory manual*. College Station, Texas: Texas A&M University.

Drost, K., Wirth, R., Košler, J., Jørgensen, H. F., & Ntaflos, T. (2012). Chemical and structural relations of epitaxial xenotime and zircon substratum in sedimentary and hydrothermal environments: A TEM study. *Contributions to Mineralogy and Petrology, 165*, 737–756. https://doi.org/10.1007/s00410-012-0833-6

Elliott, W. C., Gardner, D. J., Malla, P., & Riley, E. (2018). A New Look at the Occurrences of the Rare-Earth Elements in the Georgia Kaolins. *Clays and Clay Minerals, 66*, 245–260. https://doi.org/10.1346/CCMN.2018.064096

Ellis, E. A. (2016). Quetol 651: Not just a low viscosity resin. *Microscopy Research and Technique, 79*, 50–57. https://doi.org/10.1002/jemt.22597

Ferrari, L., Orozco-Esquivel, T., Bryan, S. E., & López-Martínez, M., & Silva-Fragoso, A. (2018). Cenozoic magmatism and extension in western Mexico: Linking the Sierra Madre Occidental silicic large igneous province and the Comondú Group with the Gulf of California rift. *Earth-Science Reviews, 183*, 115–152. https://doi.org/10.1016/j.earscirev.2017.04.006

Fisher, W. L., Galloway, W. E., Proctor Jr, C. V., & Nagle, J. S. (1970). Depositional Systems in the Jackson Group of Texas their Relationship to Oil Gas, and Uranium. The University of Texas at Austin, Bureau of Economic Geology

Franz, G., Morteani, G., & Rhede, D. (2015). Xenotime-(Y) formation from zircon dissolution–precipitation and HREE fractionation: An example from a metamorphosed phosphatic sandstone, Espinhaço fold belt (Brazil). *Contributions to Mineralogy and Petrology, 170*, 37. https://doi.org/10.1007/s00410-015-1191-y

Galloway, W. E. (1978). Uranium mineralization in a coastal-plain fluvial aquifer system; Catahoula Formation, Texas. *Economic Geology, 73*(8), 1655–1676.

Giannuzzi, L. A., Drown, J. L., Brown, S. R., Irwin, R. B., & Stevie, F. A. (1998). Applications of the FIB lift-out technique for TEM specimen preparation. *Microscopy Research and Techniques, 41*, 285–290.

Guillemette, R. N., & Yancey, T. E. (1996). Composition and Provenance of Volcanic Glass in Late Eocene Manning Formation, East-Central Texas. *GCAGS Transactions, 46*, 159–166.

Hay, D. C., Dempster, T. J., Lee, M. R., & Brown, D. J. (2009). Anatomy of a low temperature zircon outgrowth. *Contributions to Mineralogy and Petrology, 159*, 81–92. https://doi.org/10.1007/s00410-009-0417-2

Heintz, M. L., Yancey, T. E., Miller, B. V., & Heizler, M. T. (2015). Tephrochronology and geochemistry of Eocene and Oligocene volcanic ashes of east and central Texas. *GSA Bulletin, 127*, 770–780. https://doi.org/10.1130/B31146.1

Henderson, J. H., Jackson, M. L., Syers, J. K., Clayton, R. N., & Rex, R. W. (1971). Cristobalite authigenic origin in relation to montmorillonite and quartz origin

🌍 Springer

in bentonites. *Clays and Clay Minerals, 19*, 229–238. https://doi.org/10.1346/CCMN.1971.0190404

Hower, J. C., Berti, D., Hochella, M. F., & Mardon, S. M. (2018). Rare earth minerals in a "no tonstein" section of the Dean (Fire Clay) coal, Knox County, Kentucky. *International Journal of Coal Geology, 193*, 73–86. https://doi.org/10.1016/j.coal.2018.05.001

Johannesson, K. H., Stetzenbach, K. J., Hodge, V. F., & Lyons, W. B. (1996). Rare earth element complexation behavior in circumneutral pH groundwaters: Assessing the role of carbonate and phosphate ions. *Earth and Planetary Science Letters, 139*(1–2), 305–319. https://doi.org/10.1016/0012-821X(96)00016-7

Jordan, B. R., Yancey, T. E., Heinrich, P. V., Miller, B. V., & McGuire, K. (2019). The Age and Geochemistry of Volcanic Ash in the Catahoula Formation of Louisiana, Mississippi, and Texas, USA. *The Journal of Geology, 127*, 207–222. https://doi.org/10.1086/701677

Kuhn, T., Bau, M., Blum, N., & Halbach, P. (1998). Origin of negative Ce anomalies in mixed hydrothermal–hydrogenetic Fe–Mn crusts from the Central Indian Ridge. *Earth and Planetary Science Letters, 163*, 207–220. https://doi.org/10.1016/s0012-821x(98)00188-5

Li, M. Y. H., Zhou, M.-F., & Williams-Jones, A. E. (2020). Controls on the dynamics of rare earth elements during subtropical hillslope processes and formation of regolith-hosted deposits. *Economic Geology, 115*, 1097–1118. https://doi.org/10.5382/econgeo.4727

Liu, J., Song, H., Dai, S., Nechaev, V. P., Graham, I. T., French, D., & Nechaeva, E. V. (2019). Mineralization of REE-Y-Nb-Ta-Zr-Hf in Wuchiapingian coals from the Liupanshui Coalfield, Guizhou, southwestern China: Geochemical evidence for terrigenous input. *Ore Geology Reviews, 115*, 103190. https://doi.org/10.1016/j.oregeorev.2019.103190

Liu, J., Chen, Q., Yang, Y., Wei, H., Laipan, M., Zhu, R., He, H., & Hochella, M. F. (2022). Coupled redox cycling of Fe and Mn in the environment: The complex interplay of solution species with Fe- and Mn-(oxyhydr)oxide crystallization and transformation. *Earth-Science Reviews, 232*, 104105. https://doi.org/10.1016/J.EARSCIREV.2022.104105

Luther, G. W. (2005). Manganese(II) Oxidation and Mn(IV) Reduction in the Environment—Two One-Electron Transfer Steps Versus a Single Two-Electron Step. *Geomicrobiology Journal, 22*, 195–203. https://doi.org/10.1080/01490450590946022

McKenzie, R. M. (1989). Manganese oxides and hydroxides. In J. B. Dixon & S. B. Weed (Eds.), *Minerals in soil environments* (pp. 439–465). Soil Science Society of America.

McLennan, S. M. (2001). Relationships between the trace element composition of sedimentary rocks and upper continental crust. *Geochemistry, Geophysics, Geosystems, 2*(4), 1021–1024. https://doi.org/10.1029/2000gc000109

Michaelides, M. N. (2011) Depositional and diagenetic processes in the formation of the Eocene Jackson Group bentonites, Gonzales County, Texas. Master's thesis, University of Texas, Austin, Texas.

Migdisov, A., Williams-Jones, A. E., Brugger, J., & Caporuscio, F. A. (2016). Hydrothermal transport, deposition, and fractionation of the REE: Experimental data and thermodynamic calculations. *Chemical Geology, 439*, 13–42. https://doi.org/10.1016/j.chemgeo.2016.06.005

Mooney, R. C. L. (1948). Crystal structures of a series of rare earth phosphates. *The Journal of Chemical Physics, 16*, 1003. https://doi.org/10.1063/1.1746668

Namayandeh, A., Modabberi, S., & López-Galindo, A. (2020). Trace and rare earth Element distribution and mobility during diagenetic alteration of volcanic ash to bentonite in eastern Iranian bentonite deposits. *Clays and Clay Minerals, 68*, 50–66. https://doi.org/10.1007/s42860-019-00054-9

Nesbitt, H. W. (1979). Mobility and fractionation of rare earth elements during weathering of a granodiorite. *Nature, 279*, 206–210. https://doi.org/10.1038/279206a0

Nesbitt, H. W., & Young, G. M. (1982). Early Proterozoic climates and plate motions inferred from major element chemistry of lutites. *Nature, 299*, 715–717. https://doi.org/10.1038/299715a0

Ni, Y., Hughes, J. M., & Mariano, A. N. (1995). Crystal chemistry of the monazite and xenotime structures. *American Mineralogist, 80*, 21–26. https://doi.org/10.2138/am-1995-1-203

Och, L. M., Müller, B., Wichser, A., Ulrich, A., Vologina, E. G., & Sturm, M. (2014). Rare earth elements in the sediments of Lake Baikal. *Chemical Geology, 376*, 61–75. https://doi.org/10.1016/j.chemgeo.2014.03.018

Pingitore, N. E., Clague, J. W., & Gorski, D. (2018). Remarkably Consistent Rare Earth Element Grades at Round Top Yttrofluorite Deposit. *Advances in Materials Physics and Chemistry, 08*, 1–14. https://doi.org/10.4236/ampc.2018.81001

Poitrasson, F., Oelkers, E., Schott, J., & Montel, J.-M. (2004). Experimental determination of synthetic NdPO$_4$ monazite end-member solubility in water from 21to 300: Implications for rare earth element mobility in crustal fluids. *Geochimica Et Cosmochimica Acta, 68*, 2207–2221. https://doi.org/10.1016/j.gca.2003.12.010

Rasmussen, B. (2005). Radiometric dating of sedimentary rocks: The application of diagenetic xenotime geochronology. *Earth-Science Reviews, 68*, 197–243. https://doi.org/10.1016/j.earscirev.2004.05.004

Rasmussen, B., Buick, R., & Taylor, W. R. (1998). Removal of oceanic REE by authigenic precipitation of phosphatic minerals. *Earth and Planetary Science Letters, 164*, 135–149. https://doi.org/10.1016/S0012-821X(98)00199-X

Roberson, H. E. (1964). Petrology of tertiary bentonites of Texas. *Journal of Sedimentary Research, 34*(2), 401–411.

Sasmaz, A., Zagnitko, V. M., & Sasmaz, B. (2020). Major, trace and rare earth element (REE) geochemistry of the Oligocene stratiform manganese oxide hydroxide deposits in the Nikopol Ukraine. *Ore Geology Reviews, 126*, 103772. https://doi.org/10.1016/j.oregeorev.2020.103772

Sasmaz, A., Sasmaz, B., & Hein, J. R. (2021). Geochemical approach to the genesis of the Oligocene-stratiform manganese-oxide deposit, Chiatura (Georgia). *Ore Geology Reviews, 128*, 103910.

Senkayi, A. L., Dixon, J. B., Hossner, L. R., Abder-Ruhman, M., & Fanning, D. S. (1984). Mineralogy and genetic relationships of tonstein, bentonite, and lignitic strata in the Eocene Yegua Formation of east-central Texas. *Clays and Clay Minerals, 32*, 259–271.

Seredin, V. V., & Dai, S. (2012). Coal deposits as potential alternative sources for lanthanides and yttrium.

International Journal of Coal Geology, 94, 67–93. https://doi.org/10.1016/j.coal.2011.11.001

Shelyug, A., Mesbah, A., Szenknect, S., Clavier, N., Dacheux, N., & Navrotsky, A. (2018). Thermodynamics and Stability of Rhabdophanes, Hydrated Rare Earth Phosphates $REPO_4 \bullet n H_2O$. *Frontiers in Chemistry, 6*, 604. https://doi.org/10.3389/fchem.2018.00604

Shen, M., Dai, S., Graham, I. T., Nechaev, V. P., French, D., Zhao, F., Shao, L., Liu, S., Zuo, J., Zhao, J., Chen, K., & Xie, X. (2021). Mineralogical and geochemical characteristics of altered volcanic ashes (tonsteins and K-bentonites) from the latest Permian coal-bearing strata of western Guizhou Province, southwestern China. *International Journal of Coal Geology, 237*, 103707. https://doi.org/10.1016/j.coal.2021.103707

Stuckman, M. Y., Lopano, C. L., & Granite, E. J. (2018). Distribution and speciation of rare earth elements in coal combustion by-products via synchrotron microscopy and spectroscopy. *International Journal of Coal Geology, 195*, 125–138. https://doi.org/10.1016/j.coal.2018.06.001

Wanhala, A. K., Wanhala, A. K., Doughty, B., Bryantsev, V. S., Wu, L., Mahurin, S. M., Jansone-Popova, S., Cheshire, M. C., Navrotsky, A., & Stack, A. G. (2019). Adsorption mechanism of alkyl hydroxamic acid onto bastnäsite: Fundamental steps toward rational collector design for rare earth elements. *Journal of Colloid and Interface Science, 553*, 210–219.

Yan, X., Dai, S., Graham, I. T., He, X., Shan, K., & Liu, X. (2018). Determination of Eu concentrations in coal, fly ash and sedimentary rocks using a cation exchange resin and inductively coupled plasma mass spectrometry (ICP-MS). *International Journal of Coal Geology, 191*, 152–156. https://doi.org/10.1016/j.coal.2018.03.009

Yancey, T. E., & Guillemette, R. (1998). Major volcanic ash units in the late Eocene of east Texas. *GCAGS Transactions, 48*, 511–516.

Yancey, T. E., Heizler, M. T., Miller, B. V., & Guillemette, R. N. (2018). Eocene Oligocene chronostratigraphy of ignimbrite flareup volcanic ash beds on the Gulf of Mexico coastal plains. *Geosphere, 14*(3), 1232–1252. https://doi.org/10.1130/GES01621.1

Zhao, L., Dai, S., Graham, I. T., Li, X., Liu, H., Song, X., Hower, J. C., & Zhou, Y. (2017). Cryptic sediment-hosted critical element mineralization from eastern Yunnan Province, southwestern China: Mineralogy, geochemistry, relationship to Emeishan alkaline magmatism and possible origin. *Ore Geology Reviews, 80*, 116–140. https://doi.org/10.1016/j.oregeorev.2016.06.014

Zielinski, R. A. (1982). The mobility of uranium and other elements during alteration of rhyolite ash to montmorillonite: A case study in the Troublesome Formation, Colorado, USA. *Chemical Geology, 35*(3–4), 185–204.

🖄 Springer